

Chapter 4

Alleviation of Retreating Side Stall Using Active Gurney Flaps

Vasileios Pastrikakis, René Steijl, and George Barakos

Nomenclature

Latin

a	Lift slope
c	Blade mean chord [m]
u	Mean velocity of the blade section relative to the fluid [m/sec]
c_p	Pressure coefficient
c_T	Thrust coefficient
c_Q	Torque coefficient
c_t	Sectional thrust coefficient
c_m	Sectional moment coefficient
c_q	Sectional torque coefficient
L_z	Rotor loading along the span in the thrust direction [N/m]
L_m	Rotor moment loading around the blade pitch axis [N]
L_q	Rotor moment loading around the shaft axis [N]
M	Mach number
N_b	Number of blades
P_i	Ideal induced rotor power [W]
P	Actual rotor power [W]

V. Pastrikakis
Consulting Engineer, SoftInWay Switzerland GmbH
e-mail: v.pastrikakis@gmail.com

R. Steijl • G. Barakos (✉)
University of Glasgow, Glasgow, UK
e-mail: Rene.Steijl@glasgow.ac.uk; George.Barakos@glasgow.ac.uk

R	Aspect ratio of the blade
FM	Figure of merit, $FM = P_i/P$

Greek

α	Angle of incidence [degrees]
β or β_0	Flapping angles [degrees]
γ	Rotor blade Lock number
θ or θ_0	Collective angle at 75 %R [degrees]
λ	Inflow factor
μ	Advance ratio
ρ	Density [kg/m^3]
σ	Rotor solidity, $\sigma = N_b c/\pi R$

Acronyms

CFD	Computational fluid dynamics
MRB	Main rotor blade

4.1 Introduction

Losses due to flow separation are detrimental to rotor performance and normally occur at the retreating side of the rotor disc where the blade is required to operate at higher angles of attack to balance the rotor disc loads. Retreating blade stall results in highly unsteady flow and vibration. Thus, controlling the flow separation is essential. Gurney flaps are capable of providing extra lift at pitch angles below stall. Therefore, the purpose of the study is to investigate the possibility of controlling the retreating blade stall using the W3 Sokol main rotor blade as a test case.

4.2 Numerical Methods

For forward-flying rotors, the HMB2 solves the compressible flow Reynolds-averaged Navier–Stokes equations in an inertial frame of reference. The employed finite-volume discretisation accounts for moving and deforming meshes in time-accurate simulations. Consequently, a rotor in forward flight is modelled in a ‘helicopter-fixed frame of reference’, where the forward flight velocity is introduced

through the definition of the ‘free-stream’ conditions. For isolated rotors, as well as rotor/fuselage or rotor/wind tunnel cases, the rotor and rotor blade motions are then accounted for using mesh velocities. For rotor/fuselage or rotor/wind tunnel cases, the relative motion of the rotor and the fixed fuselage or tunnel is accounted for the sliding plane approach (Steijl and Barakos 2008).

4.2.1 Coupling with Structural Dynamics

A modal approach was chosen to compute the deformed shape of the blade. The final deformation is then considered as a combination of the eigenvectors of the blade. The mode shapes and frequencies are first computed using NASTRAN (2005) code. The blade structure is represented as a set of beam elements located on the elastic axis of the blade. The non-linear *PBEAM* elements of NASTRAN were used. For each section, a rigid bar (*RBAR* element) without any structural properties and rigidly linked to the chord nodes was added in front of the trailing edge and aft of the leading edge in order to assess the displacement of the blade surface. The blade lead-lag stiffness is represented as a linear elastic element.

The mode shapes and frequencies which are obtained using *NASTRAN PBEAM* beam element are the flapping and chordwise area moments of inertia and the linear mass. Other properties can be added introducing the offset between the beam element axis and the blade elastic axis as well as the radius of gyration that allows coupling between the flapwise, chordwise and torsional deformations. These data need to be specified at least at the root of the element, but can also be specified at other locations of the element.

The structural model of a blade usually contains less elements than the blade surface on the fluid mesh. Therefore, the structural solution has to be interpolated on the blade surface. The deformation of the fluid mesh is done in three main steps. Firstly, the constant volume tetrahedron (CVT) method is used to interpolate the deformed shape of the blade surface. Secondly, the block vertices are moved accordingly to the spring analogy method. Finally, the full mesh is regenerated with a transfinite interpolation (TFI). The interpolation process is described in details in Dehaeze and Barakos (2012a, b, c).

For forward-flying rotors, the modal approach is used to lower the cost of computing the blade deformations. It expresses the blade deformation as a function of the blade eigenmodes. The blade shape φ is then described as a sum of eigenvectors φ_i representing the blade displacements for each eigenmode multiplied by the coefficient α_i :

$$\varphi = \varphi_0 + \sum_{i=1}^{n_m} \alpha_i \varphi_i, \quad (4.1)$$

where φ_0 is the undeformed eigenvector. The problem is then reduced to solving for the coefficients α_i .

In the modal approach, the coefficients can be obtained by solving the differential equation:

$$\frac{\partial^2 \alpha_i}{\partial t^2} + 2\zeta_i \omega_i \frac{\partial \alpha_i}{\partial t} + \omega^2 \alpha_i = \mathbf{f} \times \varphi_i, \quad (4.2)$$

where \mathbf{f} are the external forces applied to the blade projected at each structural node, and ζ_i the structural damping coefficient.

4.2.2 Trimming Method

The trimmer used for this study is based on the blade element theory and is described by Steijl et al. (2006). The trimming method consists of an initial trim-state computation and a number of subsequent retrimming steps. The initial trim state can be obtained either offline or within the CFD solver. During retrimming, the collective pitch is updated via a Newton–Raphson process, where the simple aerodynamic model is only used to compute the derivatives of the loads with respect to control inputs. For simulations of forward-flying rotors, retrimming is carried out after completion of 1 rotor revolution using revolution-averaged integrated loads from CFD solution. The trimming method needs a target thrust coefficient C_T as input. For this study, the thrust estimate is given based on flight test data. In addition, models for the fuselage and its drag are necessary in order to compute the total drag, as a function of the advance ratio of the helicopter.

From the rotor thrust and total drag, the orientation of the tip-path plane can be obtained, i.e. the forward tilt. For a rotor at straight level conditions, the orientation of the tip-path plane can be obtained from $\sin \theta_{\text{tip}} = -D/W$, where D and W represent the total drag of the helicopter and its weight.

Assuming a fixed rotor shaft angle θ_{shaft} and known first harmonic flap coefficients β_{1s} and β_{1c} , the thrust and moment coefficients can be expressed as a function of collective and cyclic pitch angles:

$$C_T = C_T(\theta_0, \theta_{1c}, \theta_{1s})$$

$$C_{M,x} = C_{M,x}(\theta_0, \theta_{1c}, \theta_{1s})$$

$$C_{M,y} = C_{M,y}(\theta_0, \theta_{1c}, \theta_{1s}),$$

where $C_{M,x}$ and $C_{M,y}$ are the non-dimensional moments about the x -axis (rotor disc rolling moment) and y -axis (rotor disc pitching moment), respectively:

$$\begin{pmatrix} \Delta \theta_0 \\ \Delta \theta_{1s} \\ \Delta \theta_{1c} \end{pmatrix} = \begin{pmatrix} \frac{\partial C_T}{\partial \theta_0} & \frac{\partial C_T}{\partial \theta_{1s}} & \frac{\partial C_T}{\partial \theta_{1c}} \\ \frac{\partial C_{M,x}}{\partial \theta_0} & \frac{\partial C_{M,x}}{\partial \theta_{1s}} & \frac{\partial C_{M,x}}{\partial \theta_{1c}} \\ \frac{\partial C_{M,y}}{\partial \theta_0} & \frac{\partial C_{M,y}}{\partial \theta_{1s}} & \frac{\partial C_{M,y}}{\partial \theta_{1c}} \end{pmatrix}^{-1} \begin{pmatrix} C_{T,\text{target}} - C_T \\ C_{Mx,\text{target}} - C_{Mx} \\ C_{My,\text{target}} - C_{My} \end{pmatrix}. \quad (4.3)$$

The elements of the sensitivity matrix in Eq. (4.3) are the derivatives of C_T , $C_{M,x}$ and $C_{M,y}$ according to the blade element theory. Assuming a constant inflow factor λ and fixed flapping harmonics, the sensitivity matrix is:

$$\begin{pmatrix} \frac{\partial C_T}{\partial \theta_0} & \frac{\partial C_T}{\partial \theta_{1,s}} & \frac{\partial C_T}{\partial \theta_{1,c}} \\ \frac{\partial C_{M,x}}{\partial \theta_0} & \frac{\partial C_{M,x}}{\partial \theta_{1,s}} & \frac{\partial C_{M,x}}{\partial \theta_{1,c}} \\ \frac{\partial C_{M,y}}{\partial \theta_0} & \frac{\partial C_{M,y}}{\partial \theta_{1,s}} & \frac{\partial C_{M,y}}{\partial \theta_{1,c}} \end{pmatrix} = \frac{\sigma \alpha}{4} \begin{pmatrix} (\frac{2}{3} + \mu^2) & -\mu & 0 \\ \frac{2}{3}\mu & -\frac{1}{4}(1 + \frac{3}{2}\mu^2) & 0 \\ 0 & 0 & \frac{1}{4}(1 + \frac{1}{2}\mu^2) \end{pmatrix} \quad (4.4)$$

$$\begin{aligned} \delta \theta_0 &= \left[\frac{\partial C_T}{\partial \theta_0} \frac{\partial C_{M,x}}{\partial \theta_{1,s}} - \frac{\partial C_T}{\partial \theta_{1,s}} \frac{\partial C_{M,x}}{\partial \theta_0} \right]^{-1} = \left(\frac{\partial C_{M,x}}{\partial \theta_{1,s}} (C_{T,\text{target}} - C_T) + \frac{\partial C_T}{\partial \theta_{1,s}} C_{M,x} \right) \\ \delta \theta_{1,s} &= \left[\frac{\partial C_T}{\partial \theta_0} \frac{\partial C_{M,x}}{\partial \theta_{1,s}} - \frac{\partial C_T}{\partial \theta_{1,s}} \frac{\partial C_{M,x}}{\partial \theta_0} \right]^{-1} = \left(\frac{\partial C_{M,x}}{\partial \theta_0} (C_{T,\text{target}} - C_T) + \frac{\partial C_T}{\partial \theta_0} C_{M,x} \right) \\ \delta \theta_{1,c} &= -C_{M,x} / \frac{\partial C_{M,y}}{\partial \theta_{1,c}} \end{aligned} \quad (4.5)$$

Similar approaches have been used in Yang et al. (2002), Van der Ven and Boelens (2004) and Park and Kwon (2004). Yang et al. (2002) used a lifting-line technique, external to the flow solver, to obtain the derivatives of the rotor performance parameters. An alternative expensive approach is presented in Van der Ven and Boelens (2004) and Park and Kwon (2004), where the flow solver is used to determine the derivatives of the rotor performance parameters by repeating the simulation with slightly different values of the angles θ_0 , $\theta_{1,s}$ and $\theta_{1,c}$ in succession. An accurate estimate of the derivatives requires a converged flow solution for each of these different control settings. Typical trimmed rotor simulations involved up to 35 revolutions of the rotor.

4.3 W3 Main Rotor

For forward flight, a Gurney flap of 0.02c height was placed at 0.40R and had a span of 0.25R. The Gurney flap was represented in the local mesh around the blade. The mesh used for the forward flight calculations consists of 27 million nodes. It is a combined C-type topology in the chordwise plane with 402 nodes along the blade and O-type topology in the spanwise plane with 196 nodes around every section of the blade. In the normal direction of the blade, 64 nodes have been used. The domain is split in the rotor mesh which includes the rotor blade geometry and the hub and the background mesh. The flow in the interface of those two meshes is interpolated using sliding planes. The whole domain is split in 5480 blocks and it is presented in Fig. 4.1.

4.4 Flight Test Data

The flight measurements were obtained by PZL-Świdnik for four different flight cases: hover and forward flight at low, medium and high speed. A first target of

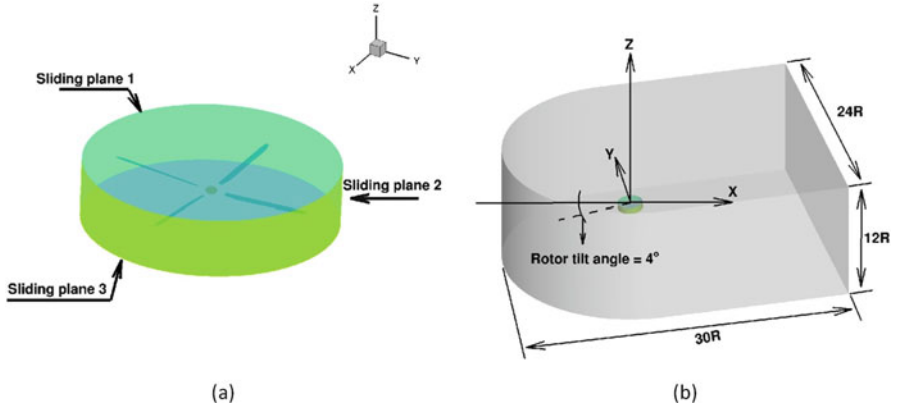
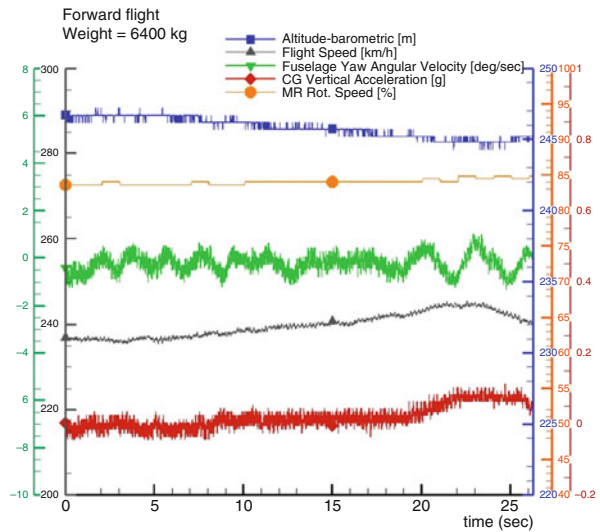


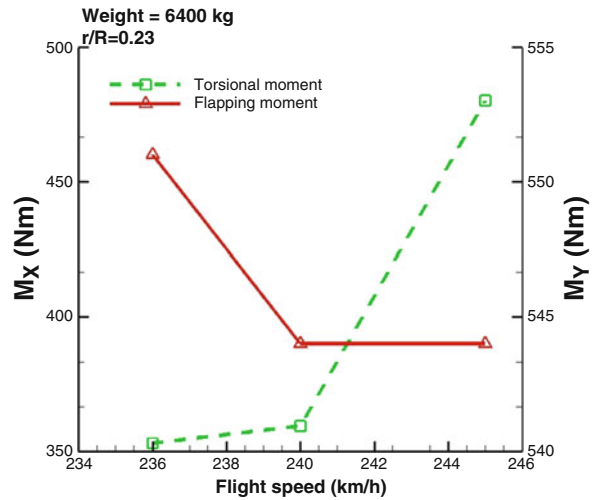
Fig. 4.1 (a) Sliding planes around W3 main rotor in forward flight and (b) overview of the computational domain used for the forward flight calculations

Fig. 4.2 Time domain flight parameters for forward flight with helicopter weight equals to 6400 kg



this work was the identification of blade stall. Data was used for a forward flight at indicated speed between 236 km/h and 245 km/h, while at the same time, the weight of the helicopter was the maximum allowed weight according to the design specifications (6400 kg), so that the indication of stall was more visible. The time domain flight parameters for that case are presented in Fig. 4.2. Figure 4.3 presents the peak to peak values for the torsional moment and the flapping bending moment at $r = 0.23R$. Figure 4.4 presents the harmonic analysis for the flap, lag and feather moments of the first blade. Based on previous flight test data processing, for a four-bladed rotor, the existence of high harmonic content frequencies which cannot be divided by 4 suggests vibrations due to stall. Table 4.1 presents the forward flight conditions of the W3 rotor.

Fig. 4.3 Peak to peak values of torsional and flapping moments at $r/R = 0.23$, helicopter weight equals to 6400 kg



4.5 Forward Flight

Figure 4.5 presents the schedule of the feathering and flap angles of the blade around the azimuth. Based on that schedule, the blade seems to operate beyond the stall limit of the NACA23012M aerofoil at the retreating side, which could be the cause for stall at inboard sections. The $k-\omega$ SST turbulence model was used and the rotor completed 4 revolutions with quarter degree steps before the loads reached convergence.

4.5.1 Rigid Blade

A separated flow region was identified at the retreating side of the rotor. Figure 4.6 presents the pressure distribution and the flowfield at 45 %R at several azimuthal positions between $\Psi = 210^\circ$ and $\Psi = 310^\circ$. Once the pressure at the leading edge of the suction side starts diverging, this is a good indication the flow separation will occur. This happens at $\Psi = 250^\circ$, and it can be seen from the streamlines and the vorticity levels near the trailing edge. The flow reattaches at $\Psi = 310^\circ$.

After processing the CFD results, Fig. 4.7 presents the stall map along with the designed actuation algorithm of the Gurney flap which had a span of $0.25R$, and its size was $0.02c$ based on the performance on the flap at the same rotor in hover. The Gurney flap is fully extracted between 200 and 300° and it is fully retracted between 30 and 120° . Figure 4.8 presents a comparison of the pressure distribution between the clean rotor and the rotor with the active Gurney as well as the flowfield for the Gurney case at inboard sections of the blade and at the retreating side of the rotor. It

Fig. 4.4 Harmonic analysis of (a) torsional, (b) flapping and (c) lagging moments of the first MRB at $r/R = 0.23$; helicopter weight equals to 6400 kg. Case conditions are presented in Table 4.1

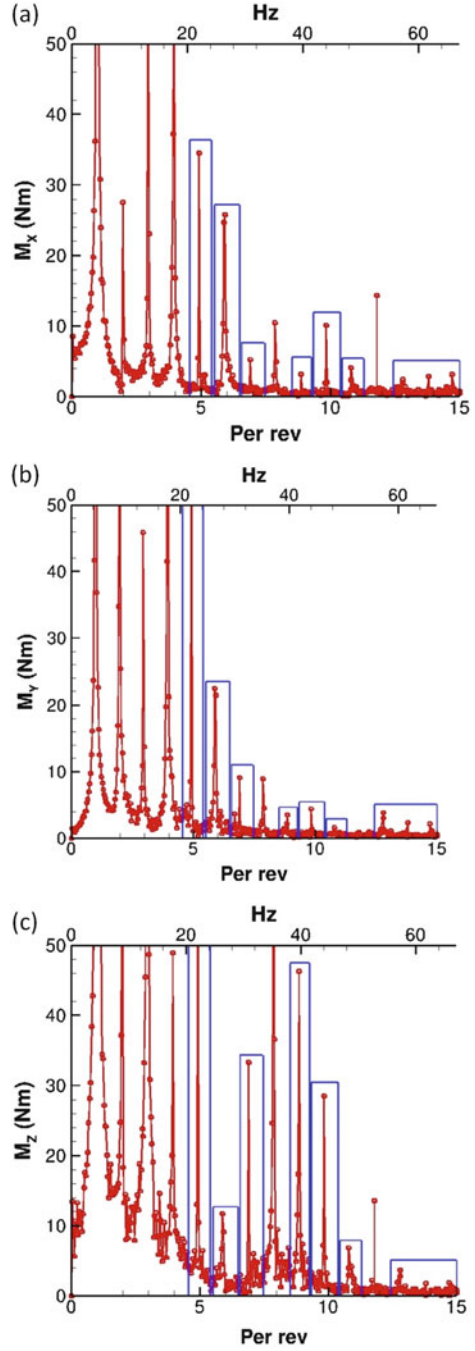
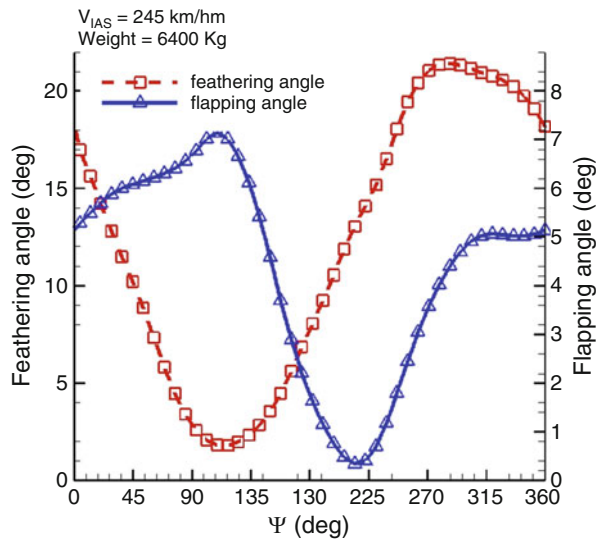


Table 4.1 Forward flight conditions for the W3 Sokol main rotor

Flight parameters	
V_{IAS}	245 km/h
M_∞	0.2052
Re_∞	1.2×10^6
μ	0.3229
θ_0	12.38°
β_0	3.55°
θ_c	-4.87°
θ_s	8.68°
β_c	-1°
β_s	-3.5°

Fig. 4.5 Schedule for the feathering and flapping angle for the W3 Sokol MRB in forward flight. Case conditions are presented in Table 4.1



is observed that the pressure coefficient diverges less if the Gurney flap is actuated indicating that the flap removed some of the stall.

Figure 4.9 presents the disc loads for the clean rotor and the rotor with the active flap along with the difference on the loads between the two cases for the rigid untrimmed rotor. The higher lift capability of the rotor when Gurney is close to full actuation is pointed out. However, the extra lift due to the Gurney flap increases the stall at the retreating side, while mostly pitch-down moments are observed at the region where the Gurney is located. The increase of the stall leads to an increase of the torque required at the same azimuthal location. When both rotors were trimmed at the same thrust setting ($C_T = 0.015$), indicative results of pressure coefficient distribution were shown in Fig. 4.10. The C_p was based on the freestream velocity, and the effect of the Gurney on decreasing the pressure on the suction side of the blade is visible. It is to be noted that the effect of the Gurney decays rapidly away from the tips of the flap.

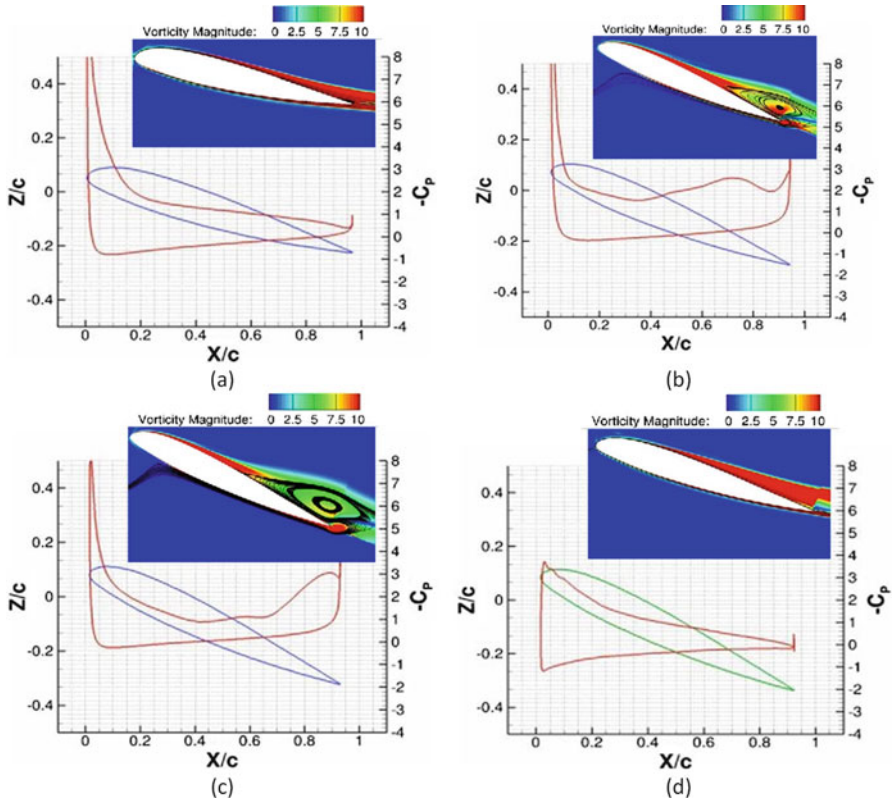


Fig. 4.6 Pressure distribution and vorticity magnitude visualisation at $r/R = 0.45$ of the W3 Sokol blade in forward flight at (a) $\Psi = 210^\circ$, (b) $\Psi = 250^\circ$, (c) $\Psi = 270^\circ$ and (d) $\Psi = 310^\circ$. Case conditions are presented in Table 4.1

4.5.2 Elastic Blade

To obtain more representative results regarding the Gurney effect on reducing the separation, both cases were treated as elastic rotors, and they were trimmed at the same thrust settings. The mode shapes of the W3 Sokol MRB based on the structural model of Fig. 4.11 were given to the solver as an initial shape of the elastic blade. Modes up to the first torsional mode were used.

The mode shapes are presented in Table 4.2, and they are mixed flapping, in-plane and torsional deformations, which made it hard to characterise them. Figure 4.12 presents the shape of the rigid and the elastic blade shapes at the back of the disc. The tip of the elastic blade is pitched down by 10° compared to the rigid, while the blade flapped upwards by almost 2° . The lagging angle was almost 3° .

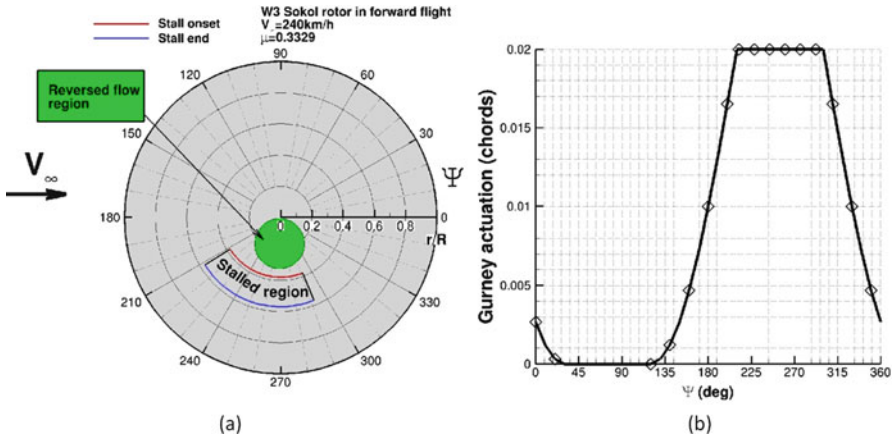


Fig. 4.7 (a) Stall map of W3 Sokol blade in forward flight and (b) actuation schedule of Gurney flap. Case conditions are presented in Table 4.1

The elastic rotor was trimmed at $C_T = 0.0117$ for both clean and Gurney cases to evaluate the effect of the flap, while the disc pitching and rolling moments were driven to zero.

Figure 4.13 presents the trimming history of the computations. For the case where the Gurney was actuated, the torque requirement of the rotor was decreased by 3.3 % (1149 kW) which corresponds to 40 KW. This reduction occurred at the retreating side of the disc because of the stall decrease.

Figure 4.14 presents streamlines near the separated region of the blade at $\Psi = 270^\circ$ along with the effect of the Gurney flap. The blade shown in Figure 4.14b is pitched down and the flow is less separated compared to the clean case. In fact, the observed benefits are due to the aerodynamic enhancement of the blade which allows the rotor to operate in lower collective, as well as the aeroelastic reshaping of the blade due to the pitching moments induced by the flap.

The increased performance of the rotor with the active Gurney flap can be evaluated using the total lift-to-drag ratio as well as the effective one as it is important to ensure that the decrease in power for the system is not due to the difference in trim state between the clean and the flapped rotor.

The effective lift-to-drag ratio is defined as: $L/D_e = L / (P/V_\infty - D)$. Based on CFD results, the drag of the clean and gurneyed rotors are 15.57 kN ($L/D = 4.03$) and 15.81 kN ($L/D = 3.97$), respectively. Thus, the effective drag for each case is $D_{e,\text{clean}} = 2.27$ kN, and $D_{e,\text{Gurney}} = 1.43$ kN, which lead to $L/D_{e,\text{clean}} = 27.66$, and $L/D_{e,\text{Gurney}} = 43.84$ (about 58 % increase compared to the clean case).

Since more data was available from flights for the W3 Sokol, CFD calculations were also performed in lower advance ratio and thrust requirements. The reason was to identify the effect of the Gurney flap along the full flight envelope of the W3 Sokol helicopter for the same actuation schedule of the flap. A complete aeroelastic trimmed computation takes about 250,000 CPU-hours to finish. The most useful

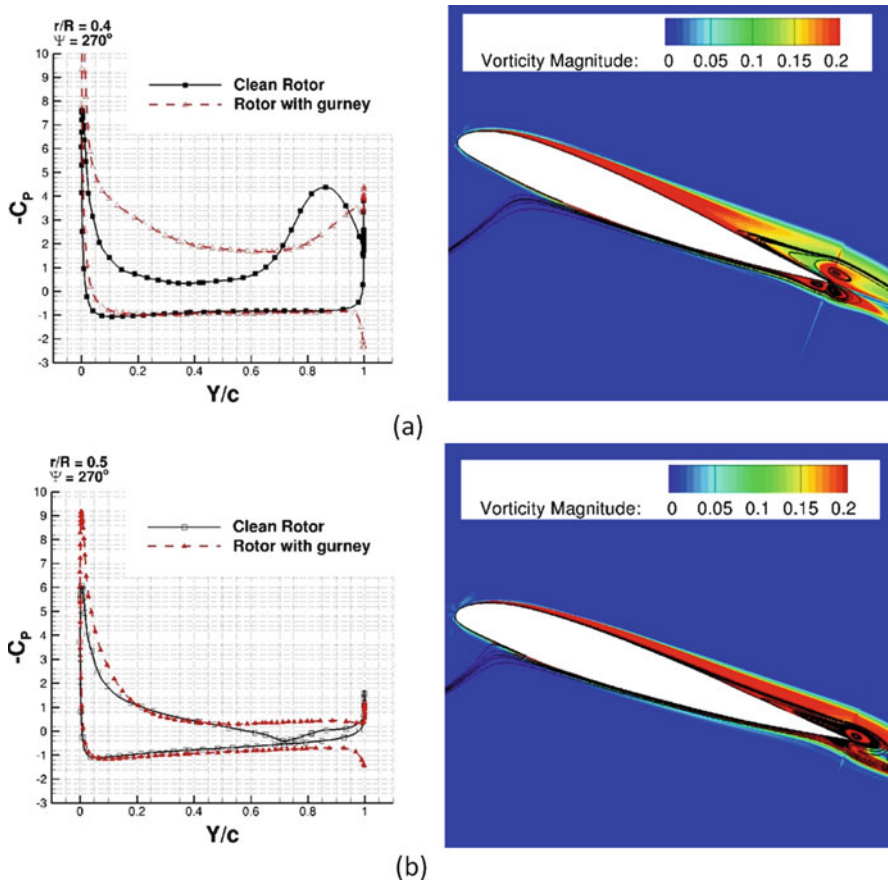


Fig. 4.8 Surface pressure coefficient and flow visualisation at $r/R = 0.4$ (a) and $r/R = 0.5$ (b). Case conditions are presented in Table 4.1

outcome of this study is the power reduction gained because of the active Gurney flap. Table 4.3 shows the effect of the flap from hover to high-speed forward flight. For this weight of the W3 Sokol, the Gurney shows some benefit in hover, although it becomes very beneficial in higher thrust requirement. During forward flight, the flap becomes beneficial close to $\mu = 0.11$. At high speed and high weight cases, the potential effect of the Gurney on the retreating blade stall alleviation enhances the aerodynamic performance of the rotor and reduces the power requirements significantly. However, Table 4.3 clearly shows that a Gurney should be deployed during hover only for high thrust requirements, while it should remain retracted at low forward flight speed.

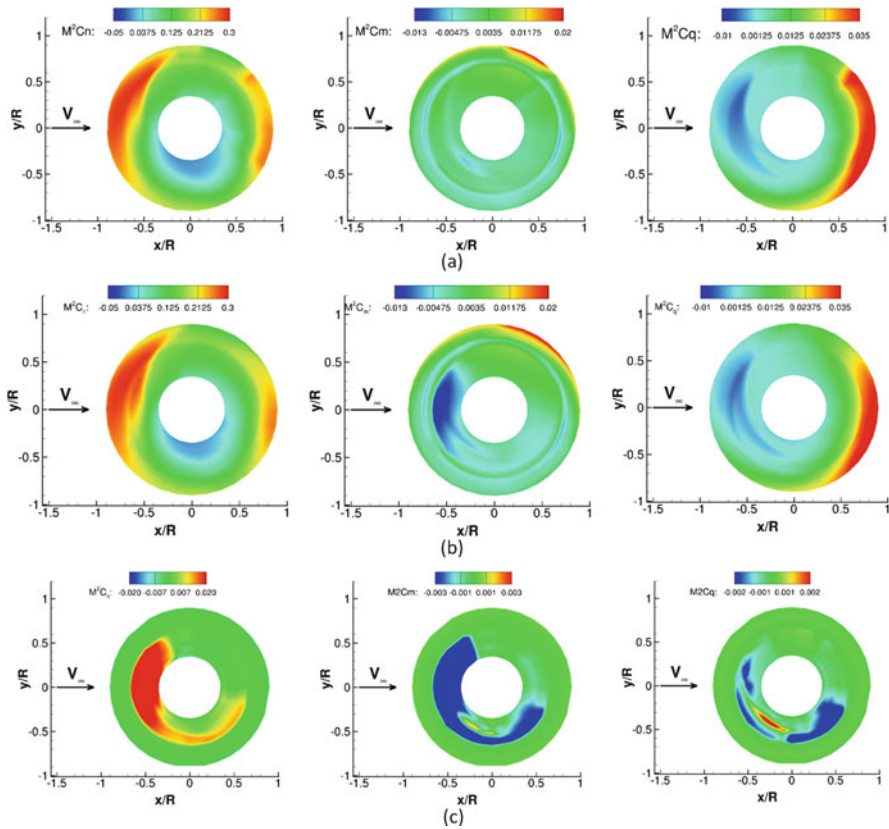


Fig. 4.9 Normal force, pitching moment and torque coefficient of the rigid untrimmed W3 Sokol MR without Gurney flap (a) and with Gurney flap (b). Load differences are presented in (c). Forward flight conditions are presented in Table 4.1

4.6 Conclusions

In this chapter, the use of a Gurney flap was put forward to improve the forward flight performance of a helicopter rotor by reducing the stall at the retreating side. The basic idea is that the flap will be actively actuated in forward flight and will be fully deployed in hover flight. The W3 Sokol MRB was used due to the availability of flight test data as well as the blade shape and structural properties. A carefully designed Gurney flap and actuation schedule proved to be essential for controlling the separation of the flow. Next, an optimisation of the Gurney location is to be considered along with closed-loop controller for the actuation of the flap. Finally, the effect of 1/rev actuation of the flap will be evaluated on the trimming and handling of a full helicopter.

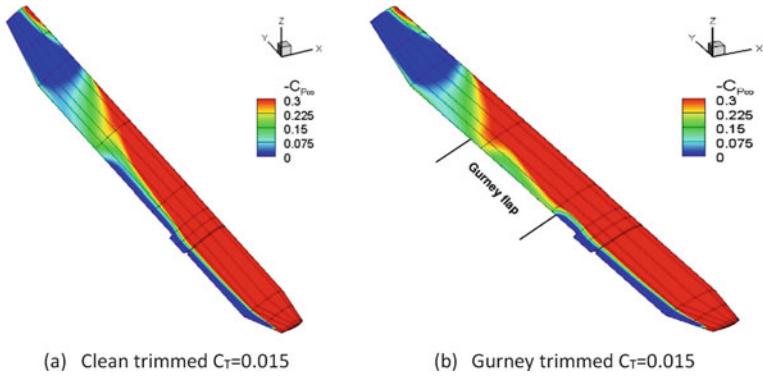


Fig. 4.10 Negative surface pressure coefficient based on the freestream velocity on clean blade (a) and (b) blade with active Gurney flap (2% of the chord) at $\Psi = 270^\circ$; both cases trimmed at $C_T = 0.015$. W3 Sokol MR in forward flight. Case conditions are presented in Table 4.1

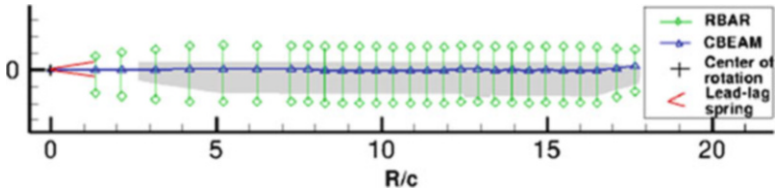
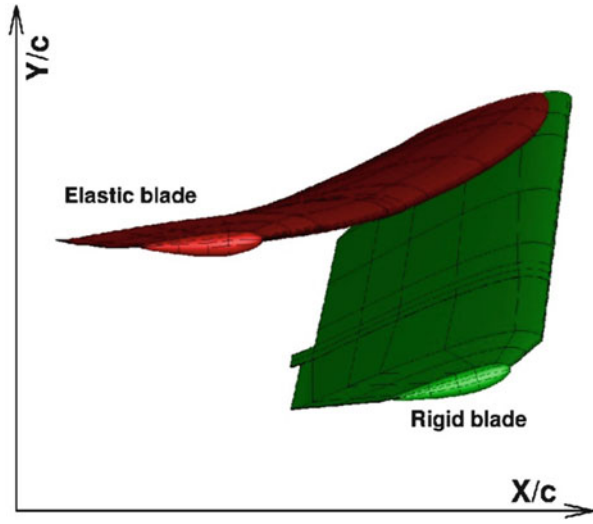


Fig. 4.11 Structural model of W3 Sokol MRB

Table 4.2 Identified modes for W3 MRB rotating at 268.485 rpm

Frequency [Hz]	Mode shape
12.17	Flapping
21.04	Flapping
21.58	In-plane
31.42	Flapping
44.02	Flapping
57.07	In-plane
60.31	Torsional

Fig. 4.12 Visualisation of the rigid and elastic W3 MRB in forward flight at $\Psi = 0^\circ$. Case conditions are presented in Table 4.1



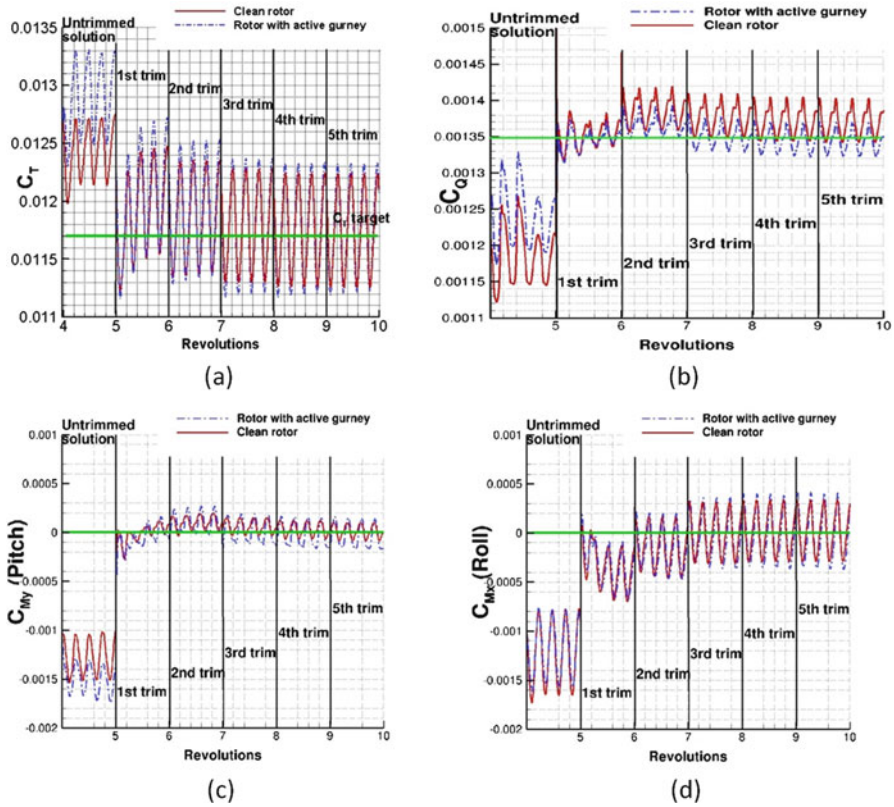
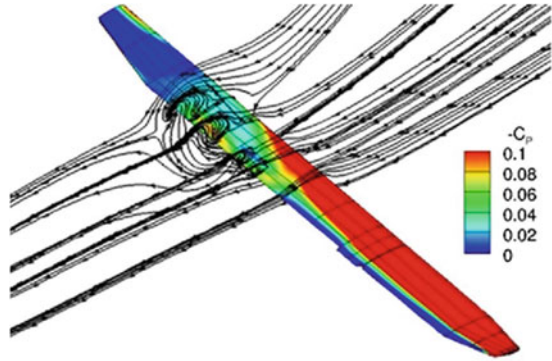
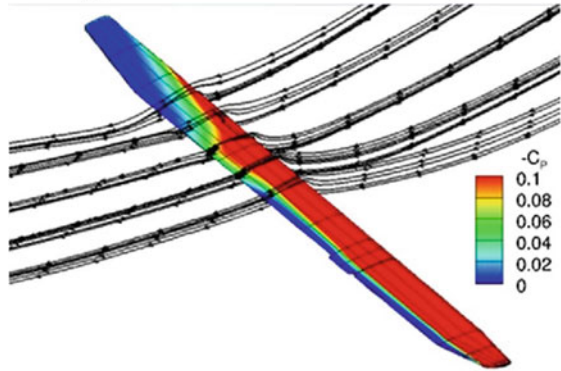


Fig. 4.13 Trimming history of (a) thrust, (b) torque, (c) rotor disc pitching moment and (d) rotor disc rolling moment of the elastic W3 Sokol MR in forward flight. Flight conditions are presented in Table 4.1

Fig. 4.14 Visualisation of the separated flow for (a) the clean blade and (b) the blade with an active Gurney flap of $0.02c$ at $\Psi = 270^\circ$ of the W3 Sokol MR in forward flight. Case conditions are presented in Table 4.1



(a) Elastic clean blade trimmed at $C_T=0.0117$



(b) Elastic blade with Gurney flap trimmed at $C_T=0.0117$

Table 4.3 Required power for clean rotor and rotor with active Gurney flap for different flight speeds and thrust settings

Advance ratio	Weight [kg]	Clean rotor—Power [HP]	Rotor with Gurney—Power [HP]	ΔP [HP]
0.0	6000	1076.7	1101.6	24.9
0.0	6400	1188.5	1205.4	16.9
0.11	6000	1034.4	1030.5	-3.9
0.11	6400	1189.6	1178.3	-11.3
0.329	6000	1365.7	1335.5	-30.2
0.3229	6400	1591.2	1542.2	-49.0

Negative ΔP indicates power benefit due to Gurney flap

References

- Dehaeze F, Barakos GN (2012) Aeroelastic CFD computations for rotor flows. In: 37th European Rotorcraft Forum, Vergiate abd Gallarate, Italy, pp 143–162
- Dehaeze F, Barakos GN (2012b) Hovering rotor computations using an aeroelastic blade model. *Aeronaut J* 116(1180):621–649
- Dehaeze F, Barakos GN (2012c) Mesh deformation method for rotor flows. *J Aircr* 49(1):82–92
- Nastran MSC (2005) Quick Reference Guide. MSC Software Corporation
- Park Y, Kwon O (2004) Simulation of unsteady rotor flow field using unstructured adaptive sliding meshes. *J Am Helicopter Soc* 49(4):391–400
- Steijl R, Barakos GN (2008) Sliding mesh algorithm for CFD analysis of helicopter rotor-fuselage aerodynamics. *Int J Numer Methods Fluids* 58(5):527–549
- Steijl R, Barakos GN, Badcock K (2006) A framework for CFD analysis of helicopter rotors in hover and forward flight. *Int J Numer Methods Fluids* 51(8):819–847
- Van der Ven H, Boelens OJ (2004) A framework for aeroelastic simulations of trimmed rotor systems in forward flight. In: 29th European Rotorcraft Forum, Marseille
- Yang Z, Sankar M, Smith M, Bauchau O (2002) Recent improvements to a hybrid method for rotors in forward flight. *J Aircr* 39(5):804–812